Phosphorylation-induced mechanical regulation of intrinsically disordered neurofilament protein assemblies

Eti Malka-Gibor, [1,†]Micha Kornreich, [1,†]Adi Laser-Azogui, [1]Ofer Doron, [1]Irena Zingerman-Koladko, [2]Ohad Medalia, [3]and Roy Beck[1,*]

[1]Raymond and Beverly Sackler School of Physics and Astronomy, Tel Aviv University, Israel
[2]Department of Life Sciences and the National Institute for Biotechnology in the Negev, Ben-Gurion University, Israel
[3]Department of Biochemistry, University of Zurich, Winterthurerstrasse 190, Switzerland

arXiv:1609.05546v1 [physics.bio-ph] 18 Sep 2016

Abstract

The biological function of protein assemblies was conventionally equated with a unique three-dimensional protein structure and protein-specific interactions. However, in the past 20 years it was found that some assemblies contain long flexible regions that adopt multiple structural conformations. These include neurofilament (NF) proteins that constitute the stress-responsive supportive network of neurons. Herein, we show that NF networks macroscopic properties are tuned by enzymatic regulation of the charge found on the flexible protein regions. The results reveal an enzymatic (phosphorylation) regulation of macroscopic properties such as orientation, stress-response and expansion in flexible protein assemblies. Together with a model explaining the attractive electrostatic interactions induced by enzymatically added charges, we demonstrate that phosphorylation-regulation is far richer and versatile than previously considered.

INTRODUCTION

In the past two decades it was discovered that approximately 50% of human proteins are intrinsically disordered, *i.e.* they contain long peptide regions that do not fold into secondary or tertiary structures. The disordered regions contain a disproportionate number of phosphorylation sites, which are functionally crucial (1). In particular, assemblies of phosphorylation-rich intrinsically disordered proteins (IDPs) are associated with neurodegenerative diseases including amyotrophic lateral sclerosis, Alzheimer's, Parkinson's and Charcot-Marie-Tooth (2–4). Despite the significance of IDP *assemblies*, little is known about the phosphorylation regulation of their structural and mechanical properties.

NFs make a valuable model system for the exploration of phosphorylation-driven interactions in IDP assemblies, due to their high modularity in protein content and phosphorylation levels. In axons, NF proteins hierarchically form a filamentous network whose main roles are to provide the cell with its mechanical support and structure (5). Protein subunits co-assemble into 10 nm bottlebrush-like filaments (Fig. 1A,B), where the filament backbone consists of the N-terminal domains. The long disordered C-terminal tail domains protrude outwards, and mediate inter-filament interactions and neuronal cytoskeletal organization (6, 7).

The expression levels of NF proteins are modified during nerve growth or trauma, where changes in protein ratios are thought to accommodate the changing mechanical and structural needs of the nervous system. This modularity is enabled by three of the NF proteins, NF-L, NF-M, and NF-H, which are expressed in both the central and peripheral nervous systems (8, 9). Their disordered tails, which govern the network organization, differ considerably in sequence, length, net charge and charge distribution (Fig. 1C-F and Table S1).

Additional functional versatility is achieved by enzymatic regulation of tail charge distribution through phosphorylation and de-phosphorylation. The majority of the phosphorylation sites correspond to the serine residues of the Lys-Ser-Pro (KSP) repeat motifs. These repeats abound in the tail domains of NF-M and NF-H subunits, and significantly alter their charges (10). For example, de-phosphorylation of NF-H tail changes its total charge from -97 to -7 e, and charge density from -0.14 to -0.01 e/amino acid (Fig. 1 and Table S1). Given this significant charge difference, NF-M and NF-H phosphorylation is thought to govern the lateral extensions of NF tails, thereby regulating NF spacing, axonal calibre and protein transport (7, 11–14). These structural roles are the focus of a recent debate, following a study that found no dependence of axonal caliber on the phosphorylation of NF-M (15).

† Eti Malka-Gibor and Micha Kornreich contributed equally to this work.
* Corresponding author: roy@post.tau.ac.il

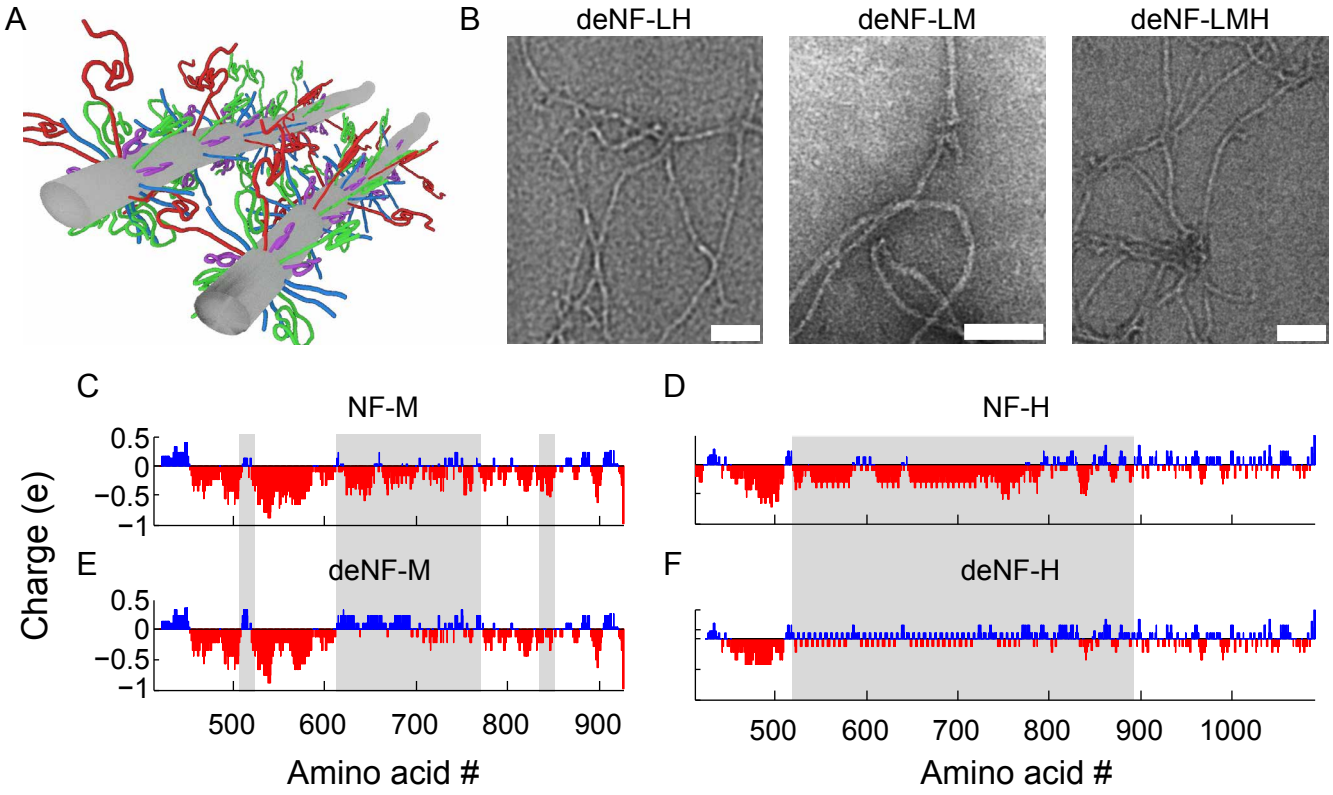

Figure 1: Structure of bottlebrush NF filaments. (A) A schematic of two neighboring interacting filaments. Each filament consists of three different subunit proteins, whose protruding tails are shown in colour (red, blue and green). (B) Transmission electron microscopy images of de-phosphorylated filaments (from left to right): NF-LH, NF-LM and NF-LMH. Scale bar = 100 nm. (c-f) Tail charge distributions of (C) phosphorylated NF-M, (D) phosphorylated NF-H, (E) de-phosphorylated NF-M, and (F) de-phosphorylated NF-H. The charge distributions were calculated at pH$= 6.8$ and averaged over a 5-amino acid window (see materials and methods). The grey boxes highlight the protein segments which are most affected by the phosphate charge removal.

Two seemingly contradictory effects can be attributed to the phosphorylation-induced charge regulation. On the one hand, phosphorylation enhances the electrostatic repulsion due to its excess charge. On the other hand, phosphorylation can promote short-range attractive cross-bridging between the disordered tails (16–21). Here we address the structural and mechanical aspects of these two opposing phosphorylation effects. We show that NF assemblies have a distinctive phosphorylation-induced regulation of network properties, such as compression resistance and orientation. The regulation stems from the structural plasticity of the disordered tails, and therefore differentiates between IDP and structured-protein assemblies.

MATERIALS AND METHODS

Calculation of basic sequence-based properties

Protein sequences are imported from UniProt database (22), and their identifiers are: P02548 (NF-L), O77788 (NF-M) and P19246 (NF-H). Since a UniProt-verified Bovine NF-H sequence is still missing, the mouse NF-H sequence is used instead. Sequence-based calculations of NF tail charge are performed at pH 6.8 using the EMBOSS amino acid pKa table (23), and the average amino acid volume $\left(V_a = 0.134\,\mathrm{nm}^3\right)$ calculation follows Ref. (24). The phosphoserine sites are determined using the UniProt database, and the phosphoserine $p\mathrm{Ka}_2$ is set to 6.2 for charge calculations. Average tail charges and tail fraction charges appear in Table S1.

Protein purification

NF subunits (NF-L, NF-M and NF-H) are purified from bovine spinal cord using a modification of an earlier protocol (25, 26). Spinal cords are homogenized in an equal volume of buffer A (0.1 M MES, 1 mM EGTA, 1 mM $MgCl_2$, 0.02% (w/v) sodium azide, 7 mM β-mercaptoethanol, *p*H 6.8 with NaOH) with 1% (w/v) Triton X-100 and 1 mM phenylmethylsulfonyl fluoride. The homogenates are centrifuged at 30k RPM (Beckman rotor type 45-Ti) for 70 min at 4 °C. An equal volume of glycerol is added to the supernatant and incubated overnight. A pellet of NFs is recovered from the glycerol solution by precipitation at 40k RPM (Beckman rotor type 45-Ti) for 90 min at 4 °C. The pellet is homogenized in buffer A with 0.8 M sucrose and clarified by spinning through a step gradient of 0.8 M sucrose buffer (0.8 M sucrose in buffer A) layered on top of 1.5 M sucrose buffer (1.5 M sucrose in buffer A) for 4 h at 55k RPM (Beckman rotor type 70-Ti). The pellet is homogenized in buffer B (0.1 M potassium phosphate and 0.1% (v/v) β-mercaptoethanol in 8 M urea, *p*H 6.5), and applied to a DEAE sepharose column (DEAE Sepharose fast flow column, GE Healthcare). The column is rinsed with buffer B containing 55 mM NaCl which elutes NF-H and protein contaminates. The next elution step, performed with buffer B at *p*H 7 containing 200 mM NaCl, elutes NF-L and NF-M. Using hydroxylapatite (HT) column chromatography (hydroxylapatite bio gel HT, Bio-Rad), the contaminants are removed from the NF-H fractions. NF-L and NF-M are separated by HT column with a gradient of 0.1 to 0.4 M potassium phosphate *p*H 7.0. The purity and separation of the NF-H, NF-M and NF-L subunit proteins are verified by SDS-PAGE (Fig. S1).

Protein de-phosphorylation

For de-phosphorylated networks, purified proteins are dialyzed against de-phosphorylation buffer (50 mM Tris *p*H=8, 100 mM NaCl and 10 mM $MgCl_2$), and then incubated with 50 units alkaline phosphatase (CIP, New England Biolabs) per 0.1 mg at 37 °C overnight. The process is monitored by the decreased mobility of de-phosphorylated NF-M and NF-H in SDS-PAGE (27, 28) (Fig. S1).

De-phosphorylation of NF-M is further supported by liquid chromatography–mass spectrometry, performed at the Biological Services Department, Weizmann institute. Technical details are found in the Supporting Material.

We compare our results against the listed NF-M phosphosites in the UniProt database. We identified 7 out of the 22 experimentally verified NF-M phosphosites, as well as 7 out of 8 of the predicted phosphosites (22). None of the sites were phosphorylated (Table S2). Notably, since bovine NF-L tails contain only few (1-3) phosphorylation sites (10), networks composed of recombinant and native NF-L proteins do not differ in inter-filament spacing, orientation or compression response (29).

Filament self-assembly and hydrogel formation

Following protein purification and de-phosphorylation, protein subunits are mixed in denaturing conditions at the desired composition. The protein solution is dialyzed against a MES buffer (100 mM MES, *p*H 6.8, 1 mM EGTA, 1 mM $MgCl_2$, 0.02% (w/v) sodium azide, 7 mM β-mercaptoethanol and a total 150 mM of NaCl and NaOH salts) at 37 °C for 48 hours.

For optical microscopy and small-angle X-ray scattering (SAXS), the reassembled filaments solution is centrifuged for 1 h at 50k RPM using a TLA120.1 rotor in a Beckman Coulter Optima TLX ultracentrifuge, and the supernatant is immediately removed from the pellet. The NF pellet is transferred to 1.5 mm quartz capillaries, overlaid with ≈100 μl MES buffer solution and sealed with epoxy glue to prevent dehydration. To osmotically pressurize the network, the overlaying MES buffer solution is supplemented with 20,000 g/mol polyethylene-glycol (PEG)(30). The resultant PEG-induced osmotic pressure Π is determined by the PEG weight percentage (PEG_{wt}), and follows the formula $\log_{10}\Pi = 1.57 + 2.75(PEG_{wt})^{0.21}$.

To determine the protein molar ratios in the assembled hydrogel, control samples are analysed by SDS-PAGE as described in Refs. (25, 29). The protein molar ratios of the different hetero-filaments are 4:1 for NF-L:NF-H (denoted NF-LH), 7:3 for NF-L:NF-M (denoted NF-LM) and 10:3:2 for NF- L:NF-M:NF-H (denoted NF-LMH).

Transmission electron microscopy

For transmission electron microscopy (TEM), a sample of 10 μl is laid on a formvar coated 400 mesh grid (#3440c-FA, SPI Supplies) and then fixed and negatively stained as in Ref. (31). Images of filaments composed of de-phosphorylated subunits are shown in Fig. 1B, and resemble images of phosphorylated protein filaments (29, 32).

Cross polarising microscopy (CPM)

The hydrogel orientation (isotropic or birefringent nematic) is characterized by crossed polarised light microscopy (Fig. 2). Sedimented NFs are observed in 1.5 mm quartz capillaries using a Nikon Eclipse LV 100 POL microscope fitted with 5-20X objectives. Micrographs are taken with a Nikon D90 camera.

Small angle X-ray scattering (SAXS)

NF hydrogels 2D diffraction data was integrated azimuthally and the intensity was plotted versus reciprocal distance q. The intensity, in arbitrary units, showed a broad peak with a maximum in the range of $q = 0.1 - 0.2\ \mathrm{nm}^{-1}$. The peak location relates to the inter-filament spacing ($d = 2\pi/q$).

Broadening of this peak is observed due to density fluctuations and the semi-flexible nature of the individual filaments. Baseline background of the form $A \cdot q^{-B} + C$ with $B = 2 - 3$ is subtracted from the integrated data, and the resultant peak is fitted with a Lorentzian function using Matlab (MathWorks) routines (32).

Preliminary experiments were performed at our home-lab using a Pilatus 300K detector and a Xenocs GeniX Low Divergence CuKα radiation source setup with scatterless slits (33). Subsequent measurements were performed at synchrotron facilities: I22 beamline in Diamond, England; SWING beamline in SOLEIL, France; and I911 SAXS beamline in MAX-lab, Sweden with 10 keV.

Bulk modulus calculations

For these calculations, we treat filament as infinitely long impenetrable cylinders of radius $R_{\mathrm{cyl}} = 5$ nm, set in a hexagonal lattice (Fig. S3 and Ref. (34)). We define a prism-shaped unit cell whose base is an equilateral triangle with side length d, which is the inter-filament distance. The prism height is l =45 nm, which is the NF protein's rod length. As 32 tails emanate from each filament backbone every 45 nm (35), the unit cell contains a total of $32/6 \cdot 3 = 16$ tails. The surface of the equilateral triangle found in the hexagonal model is $S(d) = \sqrt{3}d^2/4 - \pi R_{\mathrm{cyl}}^2/2$, and therefore the unit cell volume holds $V(d) = S(d) \cdot 45$ nm. The volume fraction is given by $\phi = NV_a/V$, where N is the number of tail amino acids in V. The Π vs. d compression curves are fitted with smoothing splines (Fig. 3), and then used for the B_T calculation:

$$B_T = -V\frac{\mathrm{d}\Pi}{\mathrm{d}V} = -S(d)\,d\frac{\mathrm{d}\Pi}{\mathrm{d}d}\left(\frac{\mathrm{d}V(d)}{\mathrm{d}d}\right)^{-1} \qquad (1)$$

RESULTS AND DISCUSSION

We investigate the mechanical and structural roles of tail phosphorylation by reconstituting filaments from purified NF protein subunit, at desired subunit compositions. To produce de-phosphorylated filaments, the natively phosphorylated proteins are enzymatically treated with alkaline phosphatase. Composite filaments include NF-L with either NF-M (NF-LM), NF-H (NF-LH) or both (NF-LMH). 10 nm wide filament formation is verified by transmission electron microscopy (TEM, Fig. 1B), as reported for native NFs (17, 36). For simplicity, we refer to the de-phosphorylated filaments by a "de" prefix (*i.e.*, deNF-LM, deNF-LH or deNF-LMH).

At high concentrations, filaments condense into a hydrogel network that phase separates from the supernatant. To characterize the mechanical response of the network, we vary the osmotic pressure (Π) using polyethylene-glycol (PEG) osmolyte. All phosphorylated filaments as well as deNF-LM filaments form large oriented (nematic) domains, either at low or high osmotic pressures, as determined by cross-polarised microscopy (CPM). In contrast, deNF-LH and deNF-LMH filaments form less oriented hydrogels with smaller nematic domains (Fig. 2). At low osmotic pressure, deNF-LH and deNF-LMH are isotropic and transition to a nematic phase at elevated osmotic pressure. Nonetheless, in both cases, even at elevated osmotic pressures, the aligned domains still appear smaller and less illuminated

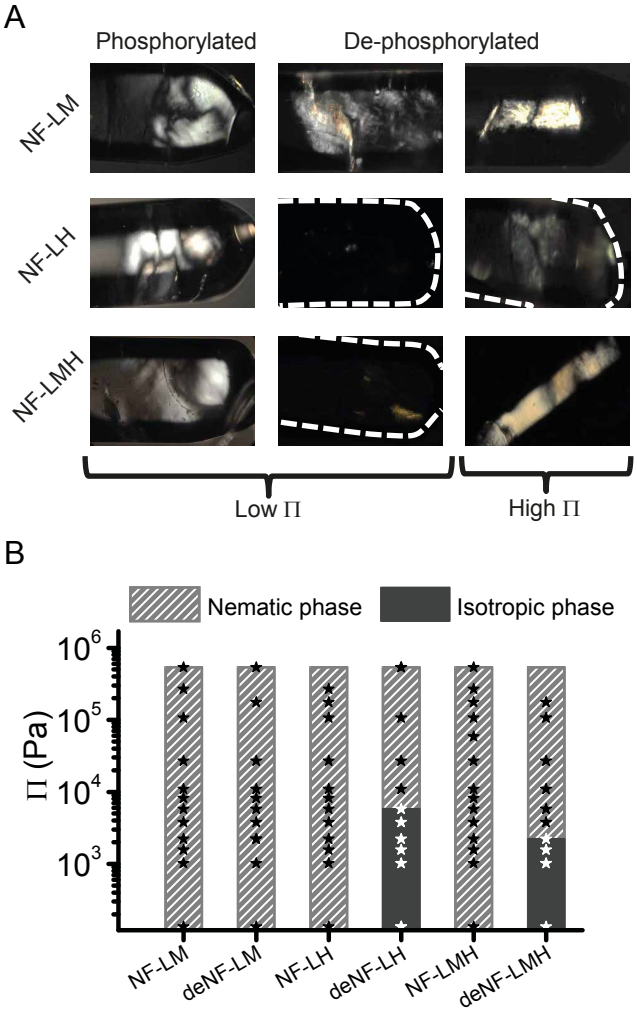

Figure 2: NF network phase behaviour, as determined by CPM. (A) Bright field and CPM images of phosphorylated and de-phosphorylated networks at low ($10^2 - 10^3$ Pa) and high ($10^5 - 2 \cdot 10^5$ Pa) osmotic pressure in quartz capillaries. White dashed lines demark the capillary boundaries, as observed with bright field (see Fig. S2). The filaments in all networks are aligned (nematic) except for deNF-LM and deNF-LMH, which are isotropic (*i.e.*, un-oriented) at low Π. Each capillary is approximately 1.5 mm wide. (B) Phase diagram showing the network phase behaviour at different Π's. Each star $\star$ denotes a measurement point.

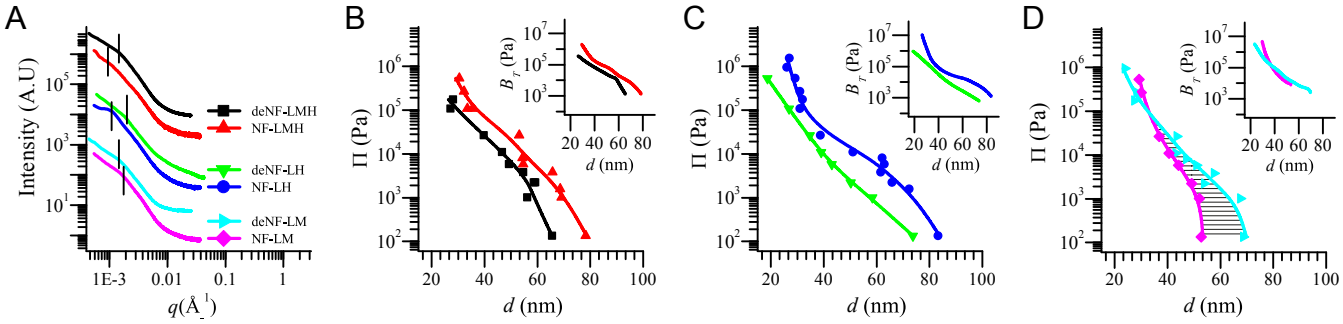

Figure 3: Comparison of native and de-phosphorylated networks using SAXS and osmotic pressure. (A) Intensity curves of NF-LH, NF-LM, and NF-LMH native and de-phosphorylated networks at 1% (w/w) PEG ($\Pi = 2.2 \cdot 10^3$ Pa). (b-d) Semi-log plot of osmotic pressure Π vs. the inter-filament distance d of different network compositions: (B) NF-LMH, (C) NF-LH and (D) NF-LM. For ϵ calculation in Eq. 2, we integrate over the textured area in (D). Osmotic bulk modulus B_T is shown in insets. The data is fitted with smoothing splines, which were then used to calculate B_T. Subunit molar ratios for native and de-phosphorylated NF-LM, NF-LH and NF-LMH filaments are 7:3 (NF-L:NF-M), 4:1 (NF-L:NF-H) and 10:3:2 (NF-L:NF-M:NF-H).

than those observed for native and deNF-LM hydrogels at comparable osmotic pressures. Hence, NF-H phosphorylation regulates the macroscopic orientation of the hydrogel networks. Furthermore, a comparison of the CPM images at various osmotic pressures indicates that deNF-M promotes orientational order while deNF-H hinders it (Fig. 2).

To study the nanoscopic structural organization and mechanics of the hydrogel, we measure the inter-filament spacing, d, using small-angle X-ray scattering (29, 32, 37). Azimuthally averaged intensity curves of phosphorylated (*i.e.*, native) and de-phosphorylated networks at $\Pi = 2200$ Pa, are shown in Fig. 3A. For each intensity curve, the correlation peak position (q_0) is denoted by a vertical line, and is related to the inter-filament distance by $d = 2\pi/q_0$. At this given osmotic pressure, de-phosphorylation of NF-LMH and NF-LH results with a decrease of the inter-filament spacing from 70 to 58 nm and from 67 to 50 nm, respectively. Therefore, native phosphorylation of NF-LH and NF-LMH results with network expansion. This agrees with the conventionally considered roles of NF phosphorylation, where the substantial addition of charged phosphate groups is naively expected to stretch the NF tails and consequently increase the inter-filament spacing. The Π vs. d curves of NF-LH and NF-LMH exhibit the same phosphorylation-dependent effect over a wider range of osmotic pressures (Fig. 3B,C).

In contrast, the correlation peak of deNF-LM shifts to lower q-values, in comparison to the NF-LM peak (Fig. 3A). This indicates that the spacing actually increases from 48 to 60 nm due to de-phosphorylation. The result is atypical of charged polymers, as de-phosphorylation reduces the net charge by $\sim 50\%$, and thus the electrostatic repulsion between adjacent filaments is expected to decrease. This behaviour indicates an attractive interaction between phosphorylated tails, which opposes the trend observed in NF-LH and NF-LMH networks (Fig. 3B,C). Notably, the expansion of deNF-LM in comparison to NF-LM is reversed only at high osmotic pressures, $\Pi \gtrsim 10^5$ Pa (Fig. 3D).

The protein-dependent regulation of network expansion, alignment and osmotic stress response is schematically summarized in Fig. 4, together with conjectured tails microscopic organization (Fig. 4C,D,F). Phosphorylation of the NF-H tail aligns the network and increases the inter-filament distance (Fig. 4A). In contrast, NF-M phosphorylation has little effect on network alignment, and it surprisingly *reduces* the inter-filament distance (Fig. 4B). This indicates that NF-LM and NF-LH tails are organized differently.

At low osmotic pressures, tails are expected to form two distinctive layers, known as the flower conformation (Fig. 4C). The inner layer corona is composed of the short NF-L tails while NF-H tails are repelled farther away from the corona into the outer layer. Since the tails within the outer layer are less dense, they assume a flower-like conformation (29, 38, 39). However, this picture does not agree with the NF-LM tails organization. The inter-filament spacing of NF-LM and NF-L networks are very similar (29, 32), suggesting that the long NF-M tails are hidden within the NF-L inner coronas (termed "truffle" regime) (29, 34). Under significant osmotic pressure, all filament types align and compress, while opposite tails increasingly inter-penetrate (Fig. 4E,F).

In living cells, the osmotic pressure is induced by the crowded environment. We note that the effect of phosphorylation on the compression response is much more pronounced than its effect on NF expansion. In particular, phosphorylation at a given osmotic pressure, does not change the inter-filament spacing by more than 25%. However, in order to maintain the same spacing at the phosphorylated state, the osmotic pressure needs to increase by up to two orders of magnitudes.

To further characterize this mechanical response, we calculate the osmotic bulk modulus, B_T, which quantifies the

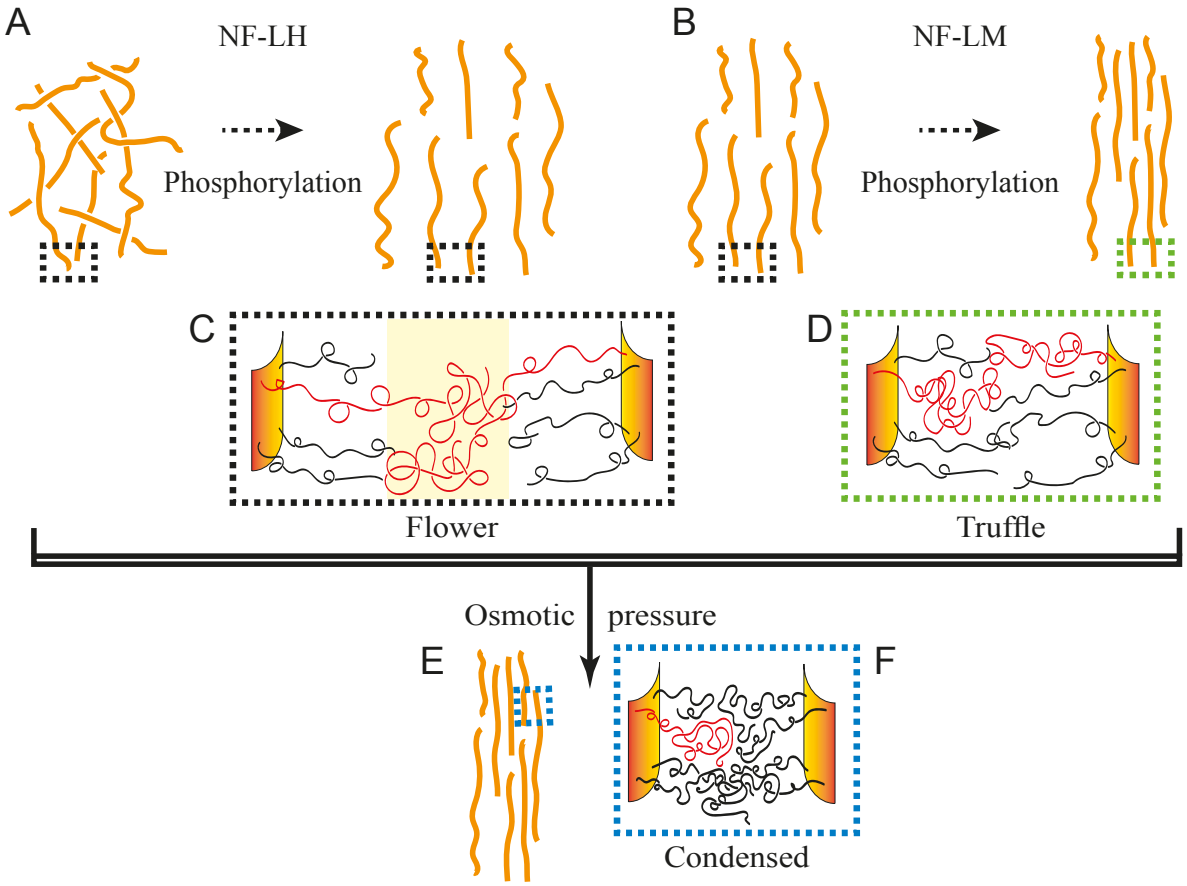

Figure 4: Schematic of phosphorylation regulation of NF network expansion, alignment and osmotic stress response. (A) NF-H phosphorlyation aligns the isotropic deNF-LH network and increases the inter-filament distance, whereas (B) NF-M phosphorylation collapses the nematic deNF-LM network. Except for NF-LM networks, all protruding tails organize in two corona layers at low osmotic pressure (C). The outer layer is formed by the long tails (either NF-H or NF-M), and is denoted by a yellow background. Upon phosphorylation, deNF-LM tails transition from a (C) flower to a (D) truffle conformation. (E) Under significant osmotic compression, filaments align and compress (F) while opposite tails increasingly inter-penetrate.

network's resistance to compression (Eq. 1 and Fig. 3B-D, insets). Similar to the phosphorylation dependent network expansion and collapse, we find that changes to the mechanical response are also protein specific. However, the effect of phosphorylation on the mechanical response is more pronounced, and B_T is altered by as much as an order of magnitude. For NF-LH and NF-LMH, de-phosphorylation of the tails reduces B_T at all d. In contrast, de-phosphorylation of NF-LM increases the network's resistance to compression (*i.e.*, larger B_T) at low osmotic pressure. The latter occurs despite the reduced repulsive electrostatic forces and suggests that the charged phosphates also take part in attractive interactions (16, 32). Further support to the excess electrostatic repulsion at high and low osmotic pressures are given by comparison to polymer scaling theories (Fig. S4).

To estimate the attractive bridging energy per NF-LM phosphosite, we follow the calculation performed to quantify the attractive hydration energy between DNA double-helices (40). The free energy is derived from the $\Pi - d$ diagram, under the hexagonal approximation. To evaluate the average energy per phosphosite (ϵ), we integrate over the free energy difference between the two phosphorylation states, and divide by the number of phosphosites in the volume (N_p):

$$\epsilon = -\frac{k_{\mathrm{B}}T}{N_p} \int_0^{\Pi_{\mathrm{int}}} \left(V_{\mathrm{deNF-LM}} - V_{\mathrm{NF-LM}}\right) \mathrm{d}\Pi. \qquad (2)$$

The integration is performed on the fitted smoothing-spline curves from $\Pi = 0$ to the intersection of the curves at $\Pi_{\mathrm{int}} \sim 10^5$ Pa (See textured area in Fig. 3D), and yields approximately $\epsilon = -8\, k_{\mathrm{B}}T$ per phosphosite. This is comparable to the free energy of protein salt bridges (41). Notably, the integration also includes contributions from repulsive

interactions, and therefore ϵ provides a lower limit for the attractive average energy per phosphosite.

Since these attractive interactions are sequence-dependent, they may account for the opposite phosphorylation expansion trends of NF-LM and NF-LH. To identify the polypeptide segments involved in such attraction, we employ a coarse-grained "handshake" calculation, aimed at locating pairs of amino acid segments that interact via electrostatic bridges (32). We calculate the unscreened Coulomb energy of two interacting segments, where each segment is centered at a specific tail amino acid and the segment length is on the order of the polypeptide persistence length (approximately 3 nm (42)). We thus obtain a 2D matrix which points at the most electrostatically viable cross-linking pairs (Fig. 5A).

Handshake analysis of the natively phosphorylated NF-H tail reveals multiple potential attractive sites located at its last 200 amino acids (Fig. 5B). This was also described by a more elaborate theoretical calculation (19) and agrees with previous experiments (43). Upon de-phosphorylation, new attractive sites are predicted near the filament backbone (Fig. 5B). These could participate in intra-filament attractive interactions, in agreement with the de-phosphorylated NF-H tail collapsed conformation (Figs. 3).

The unexpectedly collapsed conformation of phosphorylated NF-LM may involve interactions between NF-M segments with either NF-L or NF-M segments, as recently shown (29, 34). Here, upon de-phosphorylation, new NF-M attractive binding sites are formed further away from the filament backbone (Fig. 5D,E). Consequently, the loss of excess phosphate charge actually *expands* the NF-M tail, as shown in Fig. 3D.

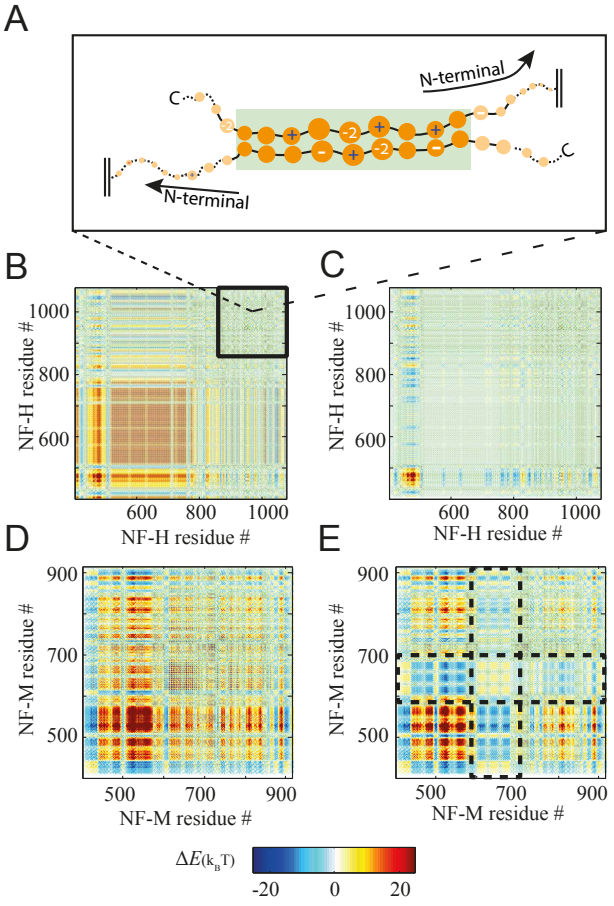

Figure 5: Handshake analysis of short-ranged electrostatic interactions between NF tail regions. (A) Two opposite 9 amino-acid long segments interacting. Details of the electrostatic interaction energy calculations are found in Refs. (29, 32). (b-e) Energy matrices for all possible segment pairs for two opposing (B) NF-H, (C) deNF-H, (D) NF-M, or (E) deNF-M tails. Interactions between two oppositely charged segments, which are more electrostatically viable, are denoted by blue colours in the interaction matrices. Solid box in (B) marks the last 200 amino-acids that are known to engage in attractive interactions. Dashed boxes in (E) denote phosphosite-rich segments (see also Fig. 1). Comparison of (D) with (E) reveals that de-phosphorylation forms new negative energy pairs between segments found further away from the filament backbone.

CONCLUSIONS

We demonstrate the roles of phosphorylation in regulating the structural and mechanical properties of NF networks. The phosphorylation-induced modifications strongly depend on the NF subunit composition, and can result with either network expansion or collapse (Fig. 4). This versatility originates from the dual nature of the induced interactions, which are both repulsive and attractive and are protein-sequence dependent.

The attractive interactions are clearly manifested in the deNF-LM network, where the removal of the excess phosphate charges unexpectedly results with network expansion. This trend relates to previous studies, which suggested that phosphorylation can promote NF binding either by associated proteins, by exposing hydrophobic residues, or by direct involvement in electrostatic bridging (16, 18, 19, 21). Of these possibilities, our results affirm the direct involvement of NF-M phosphosites in attractive interactions, which is justified by the stronger ionic bridging formed between the divalent phosphate group and basic amino acids (Fig. 5).

The repulsive interactions govern NF-LH and NF-LMH compression response. Here, phosphorylation moderately increases the inter-filament distance and considerably enhances the osmotic compression resistance, characterized by the bulk modulus (Fig. 3). This questions the hypothesized main structural role of tail phosphorylation, *i.e.* to expand the NF network, and suggests a primarily *mechanical* role to NF phosphorylation.

The individual roles of NF-M and NF-H phosphorylation, as demonstrated here, significantly increase opportunities to regulate NF network physical properties. Therefore, the roles of NF expansion (Fig. 3), mechanics (21)(Fig. 3) and orientation (44, 45)(Fig. 2) must be considered where simultaneous changes in composition and tail phosphorylation levels are observed. Such changes, for example, occur during neuronal growth and development, following injury, and in neurodegenerative diseases (8, 11, 46). Specifically, our results indicate a close relation of phosphorylation and NF compression response and orientation, which was scarcely considered before (6).

Additional assemblies of hyper-phosphorylated disordered proteins are also involved in neurodegenerative diseases. These include the disordered tau and α-synuclein proteins, which are hyper-phosphorylated in pathological inclusions (2, 3). Their aggregation is commonly attributed to an indirect process, where phosphorylation-driven conformational changes expose new segments for attractive interactions. However, the electrostatic attraction observed in phosphorylated NF-M tails demonstrates that phosphates in disordered protein assemblies *directly* engage in significant attractive interactions. This suggests that more attention should be drawn to the role of phosphorylation-driven attractive electrostatics in the study of disordered assemblies.

SUPPORTING MATERIAL

Supplement to this article is available upon request.

AUTHOR CONTRIBUTIONS

R.B, A.A.Z, E.M.G, and M.K planned and initiated the project. E.M, M.K, A.A, O.D, I.K and O.M conducted the experiments. E.M and M.K prepared the samples and analysed the data. E.M, M.K and R.B wrote the paper.

ACKNOWLEDGMENTS

We are grateful to Dr. Geraisy Wassim of Beit Shean abattoirs Tnuva for kindly providing us with the spinal cords. We thank Ekaterina Zhulina for useful discussions and suggestions. We thank the following beamlines for SAXS measurements: I911-SAXS at MAX IV Laboratory, Lund, Sweden; SWING at SOLEIL synchrotron, Paris, France; and I-22 beamline at Diamond, England. This work was supported by Israeli Scientific Foundation (571/11, 550/15) , the Tel Aviv University Center for Nanoscience and Nanotechnology and the Scakler Institute for Biophysics at Tel Aviv University. Travel grants to synchrotron facilities were provided by BioStruct-X.

References

1. Uversky, V. N., 2011. Intrinsically disordered proteins from A to Z. *Int. J. Biochem. Cell Biol.* 43:1090–1103.
2. Chen, L., and M. B. Feany, 2005. Alpha-synuclein phosphorylation controls neurotoxicity and inclusion formation in a Drosophila model of Parkinson disease. *Nat. Neurosci.* 8:657–663.
3. Stoothoff, W. H., and G. V. W. Johnson, 2005. Tau phosphorylation: physiological and pathological consequences. *Biochim. Biophys. ACTA* 1739:280–297.
4. Liu, Q., F. Xie, A. Alvarado-Diaz, M. a. Smith, P. I. Moreira, X. Zhu, and G. Perry, 2011. Neurofilamentopathy in neurodegenerative diseases. *Open Neurol. J.* 5:58–62.
5. Hirokawa, N., M. A. Glicksman, and M. B. Willard, 1984. Organization of mammalian neurofilament polypeptides within the neuronal cytoskeleton. *J. Cell Biol.* 98:1523–1536.
6. Safinya, C. R., J. Deek, R. Beck, J. B. Jones, and Y. Li, 2015. Assembly of Biological Nanostructures: Isotropic and Liquid Crystalline Phases of Neurofilament Hydrogels. *Annu. Rev. Condens. Matter Phys.* 6:113–136.
7. Sihag, R. K., M. Inagaki, T. Yamaguchi, T. B. Shea, and H. C. Pant, 2007. Role of phosphorylation on the structural dynamics and function of types III and IV intermediate filaments. *Exp. Cell. Res.* 313:2098–2109.
8. Laser-Azogui, A., M. Kornreich, E. Malka-Gibor, and R. Beck, 2015. Neurofilament assembly and function during neuronal development. *Curr. Opin. Cell Biol.* 32:92–101.
9. Yuan, A., M. V. Rao, Veeranna, and R. A. Nixon, 2012. Neurofilaments at a glance. *J. Cell. Sci.* 125:3257–3263.
10. Trimpin, S., A. E. Mixon, M. D. Stapels, M.-Y. Y. Kim, P. S. Spencer, and M. L. Deinzer, 2004. Identification of endogenous phosphorylation sites of bovine medium and low molecular weight neurofilament proteins by tandem mass spectrometry. *Biochemistry* 43:2091–2105.
11. Dale, J. M., and M. L. Garcia, 2012. Neurofilament Phosphorylation during Development and Disease: Which Came First, the Phosphorylation or the Accumulation? *J. Amino Acids.* 2012:1–10.
12. Kriz, J., Q. Zhu, J. P. Julien, and A. L. Padjen, 2000. Electrophysiological properties of axons in mice lacking neurofilament subunit genes: disparity between conduction velocity and axon diameter in absence of NF-H. *Brain Res.* 885:32–44.
13. Ackerley, S., P. Thornhill, A. J. Grierson, J. Brownlees, B. H. Anderton, P. N. Leigh, C. E. Shaw, and C. C. Miller, 2003. Neurofilament heavy chain side arm phosphorylation regulates axonal transport of neurofilaments. *J. Cell Biol.* 161:489–495.
14. Shea, T. B., C. Jung, and H. C. Pant, 2003. Does neurofilament phosphorylation regulate axonal transport? *Trends Neurosci.* 26:397–400.
15. Barry, D. M., W. Stevenson, B. G. Bober, P. J. Wiese, J. M. Dale, G. S. Barry, N. S. Byers, J. D. Strope, R. Chang, D. J. Schulz, S. Shah, N. A. Calcutt, Y. Gebremichael, and M. L. Garcia, 2012. Expansion of Neurofilament Medium C Terminus Increases Axonal Diameter Independent of Increases in Conduction Velocity or Myelin Thickness. *J. Neurosci.* 32:6209–6219.
16. Aranda-Espinoza, H., P. Carl, J.-F. Leterrier, P. Janmey, and D. E. Discher, 2002. Domain unfolding in neurofilament sidearms: effects of phosphorylation and ATP. *FEBS Letters*

531:397–401.

17. Hisanaga, S., and N. Hirokawa, 1989. The effects of dephosphorylation on the structure of the projections of neurofilament. *The J. Neurosci.* 9:959–966.
18. Gou, J. P., T. Gotow, P. A. Janmey, and J. F. Leterrier, 1998. Regulation of neurofilament interactionsin vitro by natural and synthetic polypeptides sharing Lys-Ser-Pro sequences with the heavy neurofilament subunit NF-H: Neurofilament crossbridging by antiparallel sidearm overlapping. *Med. Biol. Eng. Comput.* 36:371–387.
19. Leermakers, F. A. M., and E. B. Zhulina, 2008. Self-consistent field modeling of the neurofilament network. *Biophys. Rev. Lett.* 3:459–489.
20. Jeong, S., X. Zhou, E. B. Zhulina, and Y. Jho, 2016. Monte Carlo Simulation of the Neurofilament Brush. *Isr. J. Chem.* 56:599–606.
21. Eyer, J., and J. F. Leterrier, 1988. Influence of the phosphorylation state of neurofilament proteins on the interactions between purified filaments in vitro. *Biochem. J.* 252:655–660.
22. UniProt-Consortium, 2015. UniProt: a hub for protein information. *Nucleic Acids Res.* 43:D204–D212.
23. Hancock, J. M., and M. J. Bishop, 2004. EMBOSS (The European Molecular Biology Open Software Suite). *In* Dictionary of Bioinformatics and Computational Biology, John Wiley & Sons, Inc., Hoboken, NJ, USA.
24. Harpaz, Y., M. Gerstein, and C. Chothia, 1994. Volume changes on protein folding. *Structure* 2:641–649.
25. Jones, J. B., and C. R. Safinya, 2008. Interplay between Liquid Crystalline and Isotropic Gels in Self-Assembled Neurofilament Networks. *Biophys. J.* 95:823–835.
26. Kas, J., 1996. Mechanical Effects of Neurofilament Crossbridges. Modulation by phosphorylation, lipids, and interactions with f-actin. *J. Biol. Chem.* 271:15687–15694.
27. Carden, M. J., W. Schlaepfer, and V. Lee, 1985. The structure, biochemical properties, and immunogenicity of neurofilament peripheral regions are determined by phosphorylation state. *J. Biol. Chem.* 260:9805–9817.
28. Pant, H. C., 1988. Dephosphorylation of neurofilament proteins enhances their susceptibility to degradation by calpain. *Biochem. J.* 256:665–668.
29. Kornreich, M., E. Malka-Gibor, A. Laser-Azogui, O. Doron, H. Herrmann, and R. Beck, 2015. Composite bottlebrush mechanics: α-internexin fine-tunes neurofilament network properties. *Soft Matter* 11:5839–5849.
30. Parsegian, V. A., R. P. Rand, N. L. Fuller, and D. C. Rau, 1986. Osmotic stress for the direct measurement of intermolecular forces. *Methods Enzymol.* 127:400–416.
31. Mücke, N., L. Kreplak, R. Kirmse, T. Wedig, H. Herrmann, U. Aebi, and J. Langowski, 2004. Assessing the Flexibility of Intermediate Filaments by Atomic Force Microscopy. *J. Mol. Biol.* 335:1241–1250.
32. Beck, R., J. Deek, J. B. Jones, and C. R. Safinya, 2010. Gel-expanded to gel-condensed transition in neurofilament networks revealed by direct force measurements. *Nat. Mater.* 9:40–46.
33. Li, Y., R. Beck, T. Huang, M. C. Choi, and M. Divinagracia, 2008. Scatterless hybrid metal-single-crystal slit for small-angle X-ray scattering and high-resolution X-ray diffraction. *J. Appl. Crystal.* 41:1134–1139.
34. Kornreich, M., E. Malka-Gibor, B. Zuker, A. Laser-Azogui, and R. Beck, 2016. Neurofilaments function as shock absorbers: compression response arising from disordered proteins. *Phys. Rev. Lett.* (accepted for publication).
35. Herrmann, H., L. Kreplak, and U. Aebi, 2004. Isolation, Characterization, and In Vitro Assembly of Intermediate Filaments. Elsevier, volume 78 of *Methods Cell Biol.*, 3–24.
36. Beck, R., J. Deek, M. C. Choi, T. Ikawa, O. Watanabe, E. Frey, P. Pincus, and C. R. Safinya, 2010. Unconventional salt trend from soft to stiff in single neurofilament biopolymers. *Langmuir* 26:18595–18599.
37. Kornreich, M., R. Avinery, and R. Beck, 2013. Modern X-ray scattering studies of complex biological systems. *Curr. Opin. Biotechnol.* 24:716–723.
38. Leermakers, F. A. M., and E. B. Zhulina, 2010. How the projection domains of NF-L and alpha-internexin determine the conformations of NF-M and NF-H in neurofilaments. *Eur. Biophys. J.* 39:1323–1334.
39. Jayanthi, L., W. Stevenson, Y. Kwak, R. Chang, and Y. Gebremichael, 2013. Conformational properties of interacting neurofilaments: Monte Carlo simulations of cylindrically grafted apposing neurofilament brushes. *J. biol. phys.* 39:343–362.
40. Rau, D. C., and V. A. Parsegian, 1992. Direct measurement of the intermolecular forces between counterion-condensed DNA double helices - evidence for long-range attractive hydration forces. *Biophys. J.* 61:246–259.
41. Kumar, S., and R. Nussinov, 1999. Salt bridge stability in monomeric proteins. *J. Mol. Biol.* 293:1241–1255.
42. Bright, J. N., T. B. Woolf, and J. H. Hoh, 2001. Predicting properties of intrinsically unstructured proteins. *Prog. Biophys. Mol. Biol.* 76:131–173.
43. Chen, J., T. Nakata, Z. Zhang, and N. Hirokawa, 2000. The C-terminal tail domain of neurofilament protein-H (NF-H) forms the crossbridges and regulates neurofilament bundle formation. *J. Cell. Sci.* 113 Pt 21:3861–3869.
44. Deek, J., P. J. Chung, J. Kayser, A. R. Bausch, and C. R. Safinya, 2013. Neurofilament sidearms modulate parallel and crossed-filament orientations inducing nematic to isotropic and re-entrant birefringent hydrogels. *Nat. Commun.* 4:2224.
45. Storm, I. M., M. Kornreich, A. Hernandez-Garcia, I. K. Voets, R. Beck, M. A. Cohen Stuart, F. A. M. Leermakers, and R. de Vries, 2015. Liquid Crystals of Self-Assembled DNA Bottlebrushes. *J. Phys. Chem. B* 119:4084–4092.
46. Toman, E., S. Harrisson, and T. Belli, 2016. Biomarkers in traumatic brain injury: a review. *J. R. Army Med. Corps.* 162:103–108.